MICROSTRUCTURE AND PROCESS PARAMETERS FOR DIRECTED ENERGY DEPOSITION ADDITIVE MANUFACTUCTURING

YANIS BALIT, ERIC CHARKALUK, ANDREI CONSTANTINESCU, SYLVAIN DURBECQ

Abstract. This work studies the relationship between parameters of a *Directed Energy Deposition* process and the resulting microstructure and properties of the additively manufactured material. The results concern the analysis of single-track walls. In a first part we investigate the effect of the process parameters on the geometry of the cross section of a single-track printed on a substrate and propose an algebraic model. As a consequence we generate of an operational process parameter window for an optimal geometry. In the second part we discuss the observed microstructure under a scanning electron microscope (SEM) in terms of grain size and orientation as well as the cellular substructure. The observation observed conducts to an optimal range of the printing. The results indicate that an optimization of the process parameters trigger the control of microstructure and consequently its macroscopic mechanical behavior.

Key words: Directed Energy Deposition, process parameters, microstructure, texture, mechanical properties, etc.

1. INTRODUCTION

Additive manufacturing (AM) has been defined in [1] as: "the process of joining materials to make objects from three-dimensional model data, usually layer upon layer". This unique manufacturing technique enables the production of optimized and complex parts without the need of expensive tools such as casting molds or sophisticated machining. In the past decades, additive manufacturing has evolved from a rapid prototyping technique [2] to a manufacturing process for fully functional parts with a wide range of polymers and metallic materials [3]. Due to the low production rates and high cost per part, AM is for now a complementary technology to conventional processes and will probably never be a competitor for important series of low value components, neither for the production of very large parts. At the present moment, it is more suitable for a small number of highly complex parts and therefore, applications are the most developed in, but not limited to, aerospace [4] and biomedical industries [5].

Institut Polytechnique de Paris, Ecole Polytechnique, Laboratoire de Mécanique des Solides CNRS, France

Ro. J. Techn. Sci. – Appl. Mechanics, Vol. 64, N° 3, P. 175–188, Bucharest, 2019

The objective is to investigate the effect of the process parameters on the final properties and to associate them with the microstructure. The understanding of the underlying phenomena will demand examination at different space and time scales of the process and material. The feedstock under consideration is a standard 316 stainless steel which will be used to manufacture various single-track structure configurations. The study proposes an experimental data for the calibration of models of process parameters and track geometry. This experiment combined an in situ tensile test inside a Scanning Electron Microscope (SEM) and an Electron Backscatter Diffraction (EBSD) map. These results permitted to give a fresh analysis of the microstructure and an interpretation for monotonic tensile tests

The analysis of the process parameters begins with the presentation of the machine and the materials used in this study. Starting from an experimental database, we explore the shape of the cross section of a single-track and propose a model to predict the relation between process parameters and geometric parameters of the cross section of the track. Afterwards, we use these relations to: (i) predict the geometry of the track cross section thanks to an algebraic model, (ii) define a window of parameters for which the tracks have desired geometry. Finally, a satisfying combination of parameters was proposed and the microstructure was analyzed at two different scales.

2. MATERIALS AND METHODS

The 3D printer used in this study is the *Directed Energy Deposition* (DED) machine, denoted *Mobile* from the manufacturer BeAM, see *www.beam-machines.com*. The machine is equipped with a 500W YLR-fiber laser and the powder is delivered to the deposition region through coaxial nozzles positioned approximately 3.5 mm above the substrate surface. The laser beam was delivered to the collimator through a 200 μm optic fiber and was focused via a lens (focus length of 300 mm) on the substrate to a spot with a diameter of 0.8 mm. The operating wavelength of the laser is 1070 nm and can offer a power up to 500W. The powder is delivered by argon gas which acts also as a shielding gas around the melt pool and prevents oxidation. The material feed is controlled by the powder flow through the speed of a rotating scrapping system under the assumption that the quantity of powder is proportional to the rotation speed.

Particles fall from the scrapper in a fumer and are carried by the argon gas into the laser at the deposition zone.

As described, the precise amount of delivered particles is not directly controlled or measured by the operator and as a consequence the powder flow is delicate to fully master. The gas flow was kept constant at 6 liters per minute and a measured powder flow of 6.5 g/min, equivalent to a rotating speed of 3.3 round per minute, was used next. The 3D designed geometry is transformed into a machine readable printing code by *PowerClad, www.irepa-laser.com*. For simple geometry such as tracks or walls discussed here the G-Code was directly coded.

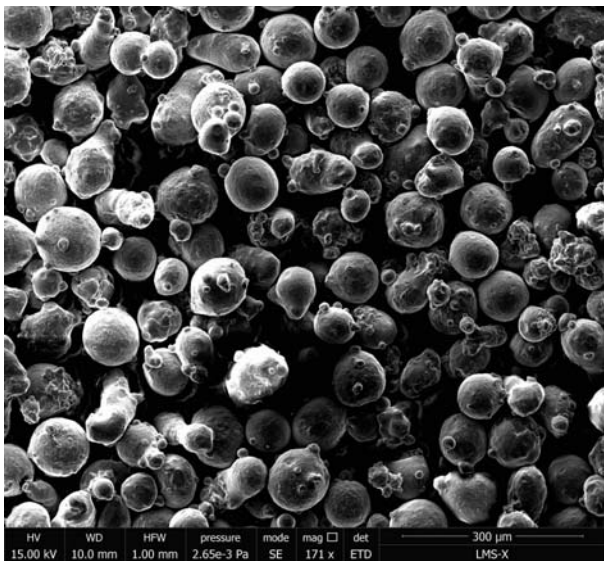

Fig. 1 – SEM image of the 316L stainless steel powder.

Austenitic stainless steels are used in a diverse range of applications. The work described here is focused on 316L stainless steel (SS316L) for the several reasons: good weldability (primordial for AM), corrosion resistance and relatively high mechanical performances, a strong interest from a wide range of industries and the availability of this material on the market.

The commercially available stainless steel 316L powder used in this study was produced through gas atomization by Höganäs AB, *www.hoganas.com*. A SEM image of the powder is proposed in Fig.1. One can observe mostly spherical particles and the satellites inherent to gas atomization. The powder particles have diameter lying within 45–90 µm and its chemical and physical properties are presented in the tables 1 and 2 respectively as extracted from the manufacturing certificate.

SS316L is after iron, primarily constituted by chromium (between 17–20%), nickel (9–14%) and molybdenum (2–4.5%), [6]. This material is composed by an Iron-Chromium-Nickel austenitic matrix i.e. a face-centered cubic (fcc) crystallographic structure and some of its minor constituents such as molybdenum, silicium, manganese act are substitution-able atoms while carbon and azote act as interstitial ones.

Table 1

Chemical Properties of the 316L stainless steel powder

Elements	C	Mo	Ni	Fe	Mn	Cr	Si
Weight (%)	0.011	2.5	12.7	balance	1.5	16.9	0.7

Table 2

Physical Properties of the 316L stainless steel powder

Apparent density (Hall)	Flowrate (Hall)
3.96 g/cm^3	18.1 s/50g

3. PROCESS PARAMETERS AND SINGLE-TRACK GEOMETRY

In the case of DED, three user accessible parameters are currently used for the control of the process: (i) the laser power P (W), (ii) the deposition speed (scanning speed, printing speed etc.) V (mm/min) and (iii) the powder flow Q (g/min). Other parameters such as spot size and energy density of the laser beam, gas flow, etc. will not be studied here, however further details can be found in [7,8,9].

Next is performed an experimental exploration of the effect of the variation of P, V and Q on the geometric parameters of a single track. The protocol consisted in printing a series of single track on a substrate, perform a transverse cut and mount each track in a polymer mold mounting for perform a fine polishing and observation as showed in Fig. 2. A standard map of cross-section of SS316L tracks manufactured by DED on SS316L substrate for a powder flow rate of 6.5 g/min are displayed in Fig. 4. as a function of the deposition speed and the laser power, the horizontal and vertical axes, respectively.

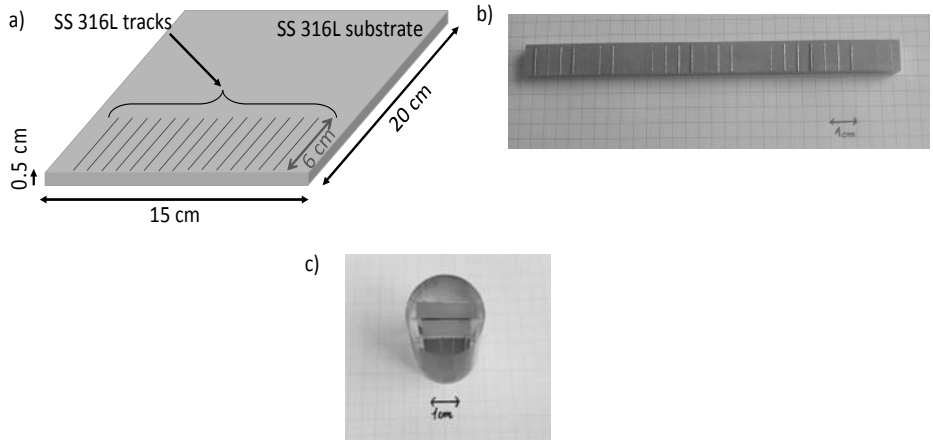

Fig. 2 – a) Schematic view of the printing procedure of SS316L tracks additively manu- factured by DED on SS316L substrate with a unique combination of the manufacturing parameters. A transverse cut was performed and tracks were separated into different mountings to perform a fine polishing as pictured in b), and c) respectively.

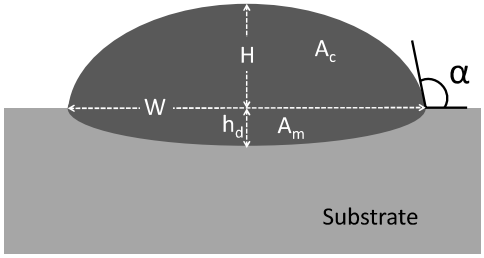

Fig. 3 – Schematic view of the cross section of a single track deposition on a substrate. Its main geometric characteristics are: track height H, track width W, track area A_c, molten area A_m, track depth h_d, track angle.

The geometry of the cross section of the track was characterized by its width W, its height H, its area A_c, the area of the molten material A_m, its depth h_d and the track angles α.

The relation between process and geometry parameters will be described using a algebraic formulae, as initially proposed in [10]:

$$\text{Geometric parameter} = a + \left(Q^{\alpha} \cdot P^{\gamma} \cdot V^{\beta}\right) + b\,,$$

where $a, \alpha, \gamma, \beta, b$ are real constants, which have been identified by least-squares.

The height of the track is directly related to the vertical increment of nozzle between two successive layers. A too large or too small vertical spacing of the nozzle leads to a large material loss during the deposition and conducts eventually to subsequent failure after a few layers. The optimal model conducted to the following formula:

$$H = 0.84 \cdot \left(Q^{0.58} \cdot P^{1.72} \cdot V^{-0.75}\right) + 42.19\,.$$

The negative value of the exponent of the deposition speed V indicates that the height diminishes for an increasing speed. One can also note the important increasing effect of the laser power as it has the highest positive exponent. The same increasing effect with a lower magnitude can be observed for the powder flow.

The optimal model for track width is:

$$W = 0.73 \cdot \left(Q^{0.15} \cdot P^{1.11} \cdot V^{-0.01}\right) + 146.01\,.$$

Let us remark, the importance of the track width both in multi-track and repaired parts, as the width assure that the printed area is filled as designed. Moreover, the exponents of the deposition speed and powder flow are small in comparison to the one of the power, indicating that the laser power drives the width

of the track. In contrast, other research groups show relations with a track width only depending on the ratio Q/P. Their relationship therefore expresses that the track is exclusively a consequence of thermal effect, i.e. the laser power and the deposition speed are both interconnected and impact the amount of energy brought per meter in the substrate and therefore on the size of the melt pool. We completely agree with the preceding observation supported by a physical interpretation, however our data did not support this conclusion.

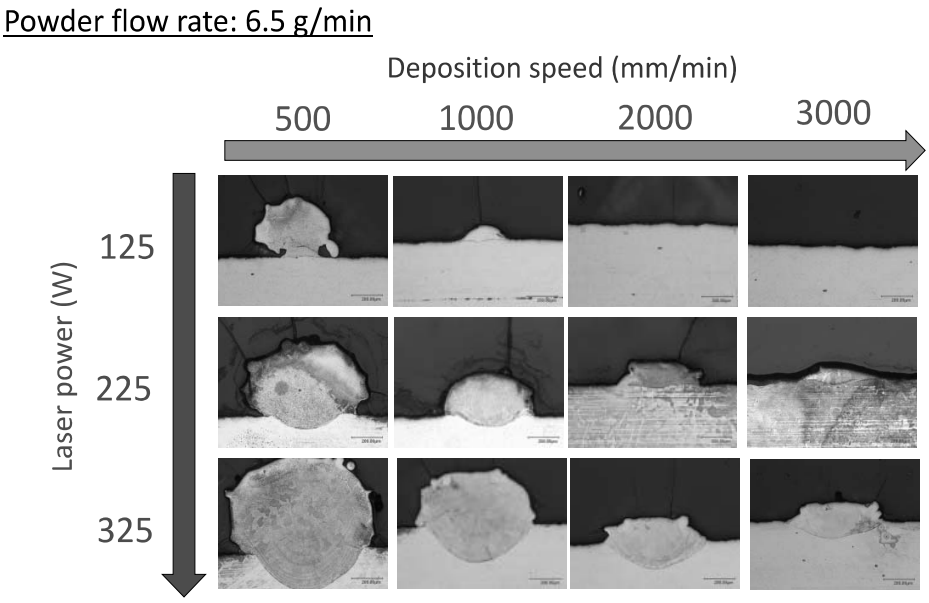

Fig. 4 – Cross-section map of SS316L tracks manufactured by DED on SS316L substrate for a powder flow rate of 6.5g/min. The deposition speed and the laser power are the horizontal and vertical axes respectively.

Further comments and correlations are present in [11]. As a illustration of the comparison between measured data and model predictions we plotted the results for three geometrical parameters in Fig. 5.

The map of process parameter is plotted in Fig. 6. The points correspond to combinations of process parameters Q, V and P and the previous parametric models serve as boundaries of the operational window in the process parameter map. The green surface is the geometrical set of process parameters defining a track with an angle of 100^{o}. Similarly, red and blue surfaces correspond dilutions of 10% and 50% respectively. The dilution D is a dimensionless parameter defined either as: (i) the ratio A_m /($A_m + A_c$), i.e. ratio of the the molten area, A_m, the sum of the molten and track area A_c [156], or (ii) by the ratio h_d / H, i.e. ratio of the track depth and height H, [12].

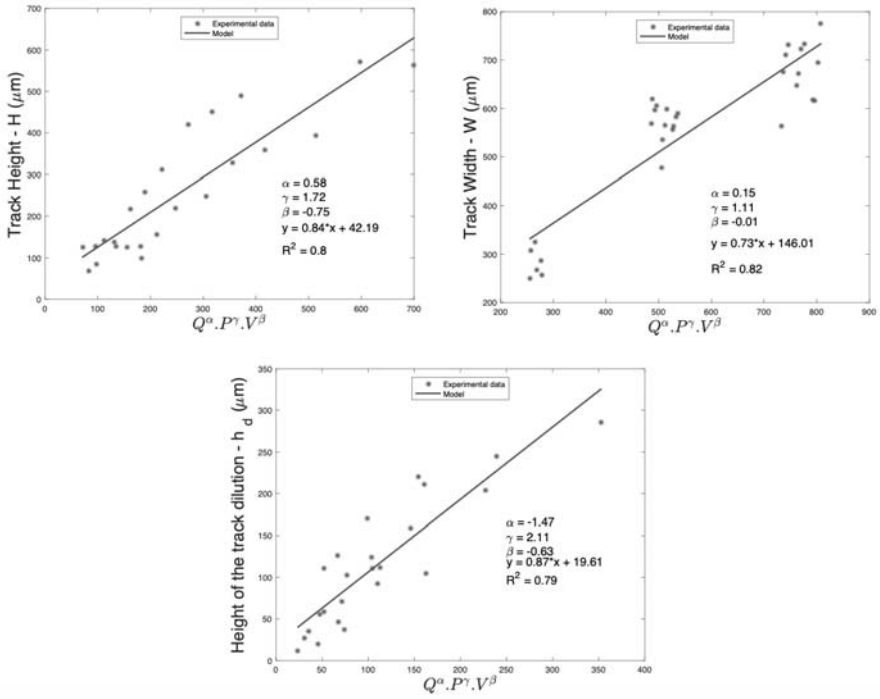

Fig. 5 – Parametric models for the height of the track dilution, the molten area and the track angle in a), b), and c) respectively.

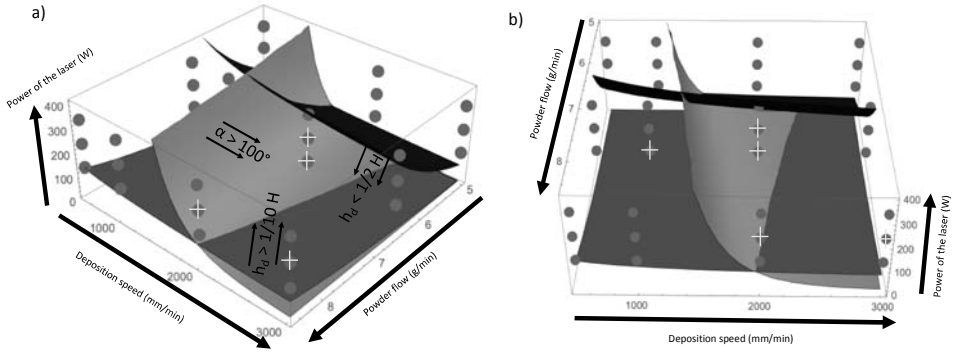

Fig. 6 – 3D process parameter map with 2 different point of view in a) and b). The blue points correspond to the combinations of parameters tested. The operational window is delimitated by the three colored surfaces. Above the green surface and the red surface, the tracks have an angle superior to 100o and a dilution superior to 10% respectively. Under the blue surface, the dilution is inferior to 50%. The yellow crosses correspond to the real combination of process parameters satisfying the requirement of geometry.

4. PROCESS PARAMETERS AND MICROSTRUCTURE

The following combination of process parameters have been used for material printing: (i) P = 225W, V = 2 000 mm/min, Q = 5 (C1) and (ii) P = 225W, V = 2 000 mm/min, Q = 6.5 (C2). The generated tracks (C1) and (C2) present a dilution of 36% and 14% respectively and also a track angle of 121.5° and 145° respectively and satisfy the dilution and track angle requirements for both repair and manufacturing.

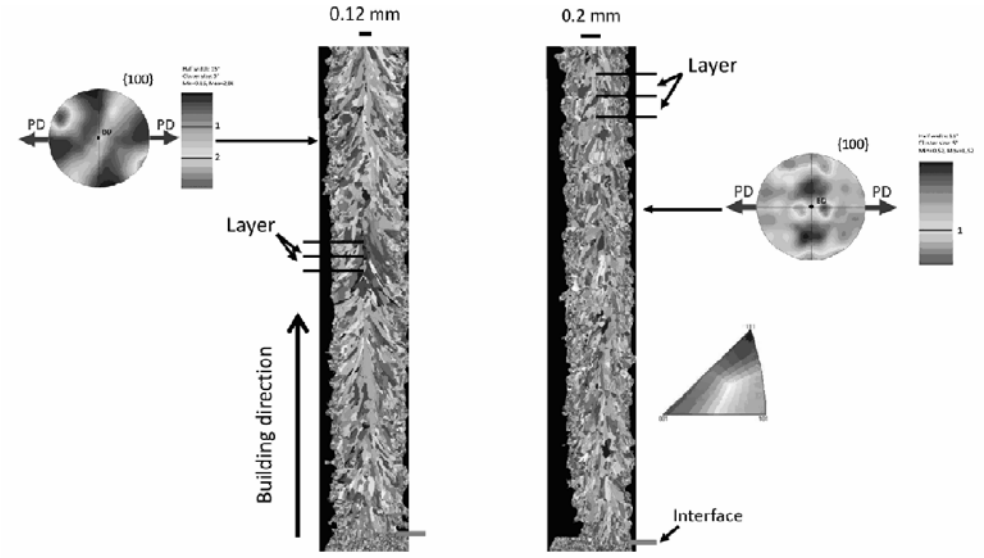

Fig. 7 – EBSD of the cross sections of two repair specimens fabricated with vertical spacings of 0.12 mm and 0.2 mm respectively. EBSD presents the position of the interfaces between layers, cluster of small grains and the firtree structure of large grains. The Pole Figures present the orientation of the grains for whole EBSD, for the layers printed from left to right and the one printed from right to left.

An EBSD image of the microstructure of the cross-sections of the single-track walls in the case of a repair specimen is represented in Fig. 7. The two repair specimens were fabricated with vertical spacing of 0.12 mm and 0.2 mm respectively. The EBSD permits to locate the the position of the interfaces between deposition layers, cluster of small grains at the surface and between the interfaces and the firtree structure of large grains in the center of the specimen. The pole figures represent the orientation of the grains for whole EBSD and for the layers printed from left to right and the one printed from right to left, which clearly indicates and influence of the process parameters. More precisely, the process parameters will affect the temperature spatial and temporal distribution and gradients and therefore will influence directly the solidification and crystallization process and the resulting morphology. A close inspection of the microstructure

exhibits an important surface covered by large grains. They mainly form the printed layers while smaller grains will cover the interface between the layers. The smaller grains will equally cluster between layer, however a repetitive pattern of the small grain clusters could not be found. A detailed statistical analysis of the microstructure for the present materials is discussed in details in [10, 12].

Similar observations on the presence of small grains and their clustering between layers were also reported in [14]. More precisely, the authors related this type of microstructure to particular values of the solidification rate and the thermal gradient associated with the heat suction from the substrate and the printing parameters. They reported that after a specific building height, the fine grains tend to disappear because of the heat accumulation in the built part, which corresponds to our observations. It has also been previously reported in [15], that grains at the top of the wall are larger than the ones at the bottom. This was associated to a faster cooling closer to the substrate. However, this was not observed in the present work as the studied surface was too small and positioned at the center of the wall. A complete discussion of the influence of the printing parameters on the texture of the morphology for an Inconnel 725 has been proposed in [16].

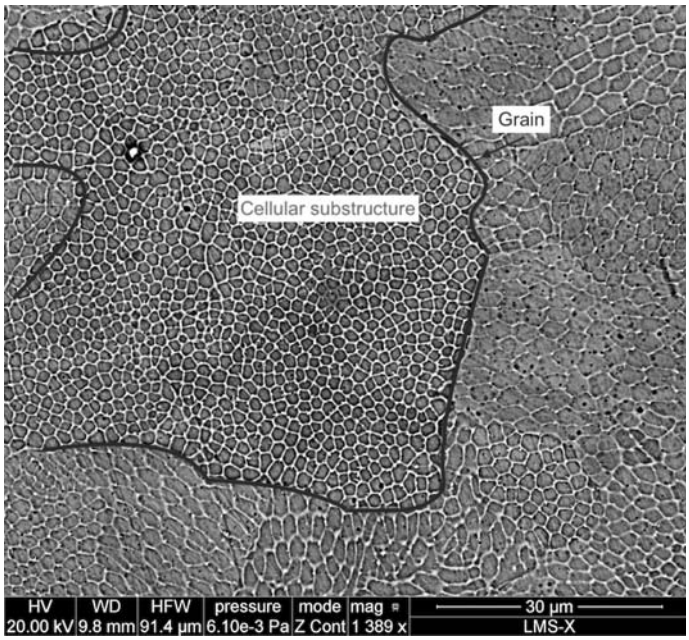

Fig. 8 – SEM image of a cross section of a track attacked by a chemical solution which highlight the presence of the cellular substructures in the grains.

After the rapid analysis of the microstructure at the level of the grains, i.e. with a mean diameter of approximatively 25 µm, let us make a rapid incursion in

lower scales. To our knowledge, a very limited number of articles dealing with the substructure in the grains were published so far at the moment of the investigation. Let us notice that the presence of cellular substructures is commonly reported for additively manufactured specimens, however a limited literature is available on their chemical composition [17, 18].

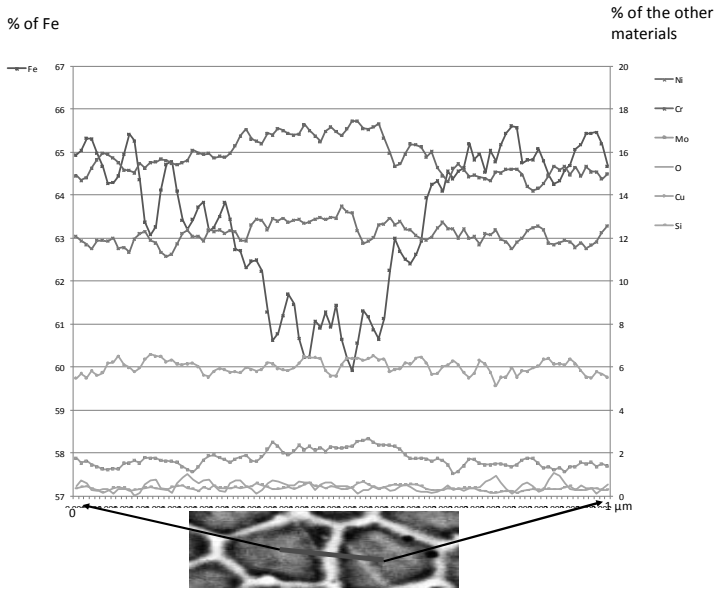

Fig. 9 – TEM Chemical analysis showing a finer state of the chemical segregation. The analysis was performed on a thin foil perpendicular to the segregation as presenter in red.

The cellular substructure was revealed by a chemical attack, composed of 80 ml HCl, 80 ml H2O and 14 g CuSO4, on the surface of the cross section of the track. A track printed with P = 325W, V = 2 000 mm/min, Q = 6.5 g/min was analyzed under a SEM. The resulting back-scattered electrons image is presented in Fig. 8. The gray levels of the image can be interpreted as follows: back-scattered electrons are sensitive to the atomic number i.e. the heavy elements appear brighter in the image and therefore the sub-cellular structure should be composed of heavier elements. To further elucidate this interrogation, we performed at first a SEM dispersive X-ray spectrometry analysis. More precisely, a linear chemical analysis was able to capture the decreasing of iron (Fe) contents in the walls. A finer Transmission Electron Microscopy (TEM) dispersive X-ray spectrometry analysis at the nanometric scale was further performed and the results are plotted in Fig. 9.

A thin foil perpendicular to the cell, represented by the red segment, was extracted. The evolution of the elements has a similar trend as exhibited in the SEM analysis concerning the presence of iron, Fe. Increasing values of Molybdenum and

Chromium, Mo and Cr respectively, have been measured which are an additional argument to explain the brightness of the cells. Similar results were reported in [17,18,19]. In [18], the presence of the elements was justified by the chemical segregation. More precisely, the slow kinetic of homogeneous alloying elements such as Molybden and Chromium conducts to the formation of the cell boundaries during the fast solidification during the printing. Furthermore, observation in [17,9] associated the cell walls with the presence of dense dislocation tangles and proposed an explanation of the enhanced strength and ductility observed during a monotonic test.

5. PROCESS PARAMETERS AND MACROSCOPIC PROPERTIES

The single-track thickness walls were built employing a back-and-forth laser scanning strategy in the printing direction. In the building direction, the vertical spacing between the successive deposited layers was of 0.12 mm and 0.2 mm. The position of the walls in the printer and the extracted dog-bone specimens are displayed in Fig. 10. The extraction of dogbone shaped specimens used for observation and testing was performed by water jet cutting and were grinded and polished.

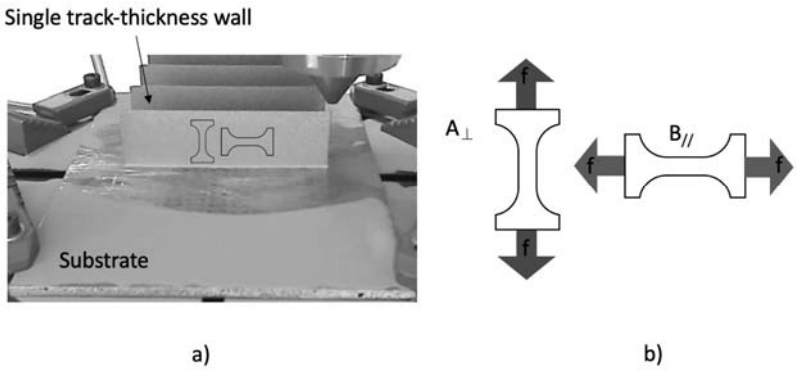

Fig. 10 – Single track thickness walls and the extracted specimen: a) positioning of the specimens in the machine with a vertical building direction and horizontal back and forth printing direction, and b) loading directions of the two specimen types.

The tensile engineering stress versus strain curve of the specimen A and B, oriented perpendicular and along the writing direction respectively and two vertical writing increments DZ of 0.2 and 0.12 mm are compared in Fig. 11. One can remark that elastic properties are isotropic for all specimens, whether plastic properties present an anisotropy for both vertical increments. However, the difference is smaller for the smaller vertical increments, as justified by the less textured microstructure, with less elongated grains, of this specimen as already noticed in Fig. 7. In addition, one can also notice that the vertical increment will

impose different linear heat inputs and consequently melt pools, cooling rate leading to a different microstructure as discussed earlier. Regarding the difference between the loading directions in specimens A and B, i.e. orthogonal or along the writing direction, we recommend the interested reader our paper [13], were the deformation pattern at the scale of the microstructure.

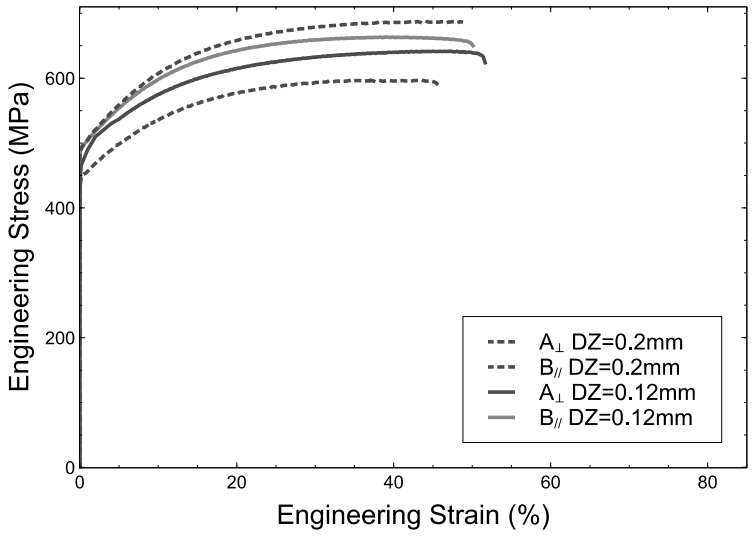

Fig. 11 – Tensile stress-strain curves for the two specimens A and B and two vertical writing increments DZ of 0.2 and 0.12 mm respectively.

In order to provide a precise quantitative comparison of the tensile response differences, we provide standard material parameters such as the yield stress at 0.2% (YS), ultimate strength (UTS) and the ductility (*D*). To facilitate the analysis, the ratio $R = R_B / R_A$ of the material parameters is compared to values from literature [20,21,22]. The ratios of YS, UTS and D in two directions of hot roled specimens present in [22] are close to 1 within 3%. Similar ratios YS, UTS and *D* for the single-track wall specimens of this study presented maximal value for the DZ = 0.2 MM wall of 1.4, 1.18 and 0.96 respectively. YS, UTS and *D* values for printed single track wall and bulk specimens from [20] and [21] reached values of 1.6, 1.19, 0.46 and 1.2, 1.1, 0.72, respectively. These results prove that similar anisotropy trends can be observed independently of the additive manufacturing process.

6. CONCLUSIONS

The paper analyzed the effects of process parameters on single-track thickness walls were built employing a back-and-forth laser scanning strategy in the printing direction on Directed Energy Deposition additive manufacturing machine.

We proposed parametric models, based on an experimental data base, characterizing the geometric parameters of the track from: Q the powder flow, P the laser power and V the deposition speed. These relations were used to predict the shape of the track above the surface and also to define an operational process parameter window in which the tracks have an optimal shape.

A combination of parameters was selected and an analysis of the microstructure at the grain and subgrain scales was performed. Grains were found to grow by epitaxy from the substrate with an elongated shape. At a smaller scale, substructures were observed and a chemical analysis showed a chemical segregation with a loss of Iron and a gain of Molybdenum and Chromium. In the literature, these cells were associated with the presence of dense dislocation tangles and were an explanation of the enhanced strength and ductility observed during monotonic test of additively manufactured specimen.

The results show that the understanding of certain phenomena can be refined. For example, proposing a dimensional analysis, directly coupling the process parameters with the temperature distribution and the cooling rates in the part or even with the statistics of the microstructure.

Acknowledgements. The authors gratefully acknowledge the financing by the DGA (France) and the SNCF (France) of this study. The authors would like to thank Louis Romain Joly (SNCF) and Marie-Christine Sainte Catherine (DGA) for fruitful discussions on the subjects, as well as Pascal Marie, Alexandre Tanguy, Simon Hallais for accompanying the printing of the structures and the SEM measurements.

Received on December 10, 2019

REFERENCES

1. ASTM International, *Standard terminology for additive manufacturing technologies*, Technical report, ASTM International, 2012.
2. MIRANDA, R.M., LOPES, G., QUINTINO, L., RODRIGUES, J.P., WILLIAMS, S., *Rapid prototyping with high power fiber lasers*, Materials and Design, **29**, *10*, pp. 2072–2075, 2008.
3. GUO, N., LEU, C.M., *Additive manufacturing: technology, applications and research needs*, Frontiers of Mechanical Engineering, **8,** *3*, pp. 215–243, Sep 2013.
4. LIU, R., WANG, Z., SPARKS, T., LIOU, F., NEWKIRK, J., *Aerospace applications of laser additive manufacturing*, In Milan Brandt (Editor), *Laser Additive Manufacturing, Woodhead Publishing Series in Electronic and Optical Materials*, Woodhead Publishing, 2017, pp. 351–371.
5. PRABHA NARRA, S., MITTWEDE P., DEVINCENT WOLF S., URISH, L.K., *Additive manufacturing in total joint arthroplasty*, Orthopedic Clinics of North America, **50,** *1*, pp. 13–20, 2019, New Technologies.
6. CUNAT, P.J., *Aciers inoxydables: critères de choix et structure. Technical report*, Les techniques de l'ingénieur, 2003.
7. ZACHARY, R.F., *The Effects of Laser and Electron Beam Spot Size in Additive Manufacturing Processes*, 2017.
8. METEL, A., STEBULYANIN, M., FEDOROV, S., OKUNKOVA, A., *Power density distribution for laser additive manufacturing (slm): Potential, fundamentals and advanced applications*, Technologies, **7**, *1*, 5, 2018.

9. FERRAR, B., MULLEN, E., JONES, E., STAMP, R., and SUTCLIFE, C.J., *Gas flow effects on selective laser melting (slm) manufacturing performance*, Journal of Materials Processing Technology, **212**, *2*, pp. 355–364, 2012.
10. COSTA, L., FELDE, I., RETI, T., KALAZI, Z., LOLACO, R., VILAR, R., and VERO, B., *A simplified semi-empirical method to select the processing parameters for laser clad coatings*, Materials Science, Testing and Informatics I, Materials Science Forum, **414**–**415**, pp. 385–394, Trans Tech Publications Ltd, 12, 2002.
11. BALIT, Y., *Mechanical properties of additively manufactured or repaired single-track thickness structures by Directed Energy Deposition*, PhD Thesis, Ecole Polytechnique, France, 2020.
12. BRUCK, G. J., *High-power laser beam cladding*, JOM, **39**, *2*, pp. 10–13, Feb 1987.
13. BALIT, Y., CHARKALUK, E., CONSTANTINESCU, A., *Digital image correlation for microstructural analysis of deformation pattern in additively manufactured 316L thin walls*, Additive Manufacturing, **31** (2020) 100862.
14. ONUIKE, B., BANDYOPADHYAY, A, *Additive manufacturing in repair: Influence of processing parameters on properties of inconel 718*, Materials Letters, **252**, pp. 256–259, 2019.
15. WANG, Z., PALMER, A. T., BEESE, M. A., Effect of processing parameters on microstructure and tensile properties of austenitic stainless steel 304l made by directed energy deposition additive manufacturing, Acta Materialia, **110**, pp. 226–235, 2016.
16. GUEVENNOUX, C., HALLAIS, S., CHARLES, A., CHARKALUK, E., CONSTANTINESCU, A., Influence of interlayer dwell time on the microstructure of Inconel 718 Laser Cladded components, submitted to Optics & Laser Technology, 2019.
17. WANG, Y. M., VOISIN, T., MCKEOWN, T. J., YE, J., CALTA, N., LI, Z., ZENG, Z., ZHANG, Y., CHEN, W., ROEHLING T. T., OTT, R. T, SANTALA, M., DEPOND, P., MATTHEWS, M., HAMZA, A., ZHU, T., Additively manufactured hierarchical stainless steels with high strength and ductility, Nature Materials, **17**, pp. 63–71, 2017.
18. SAEIDI, K., GAO, X., LOFAJ, F., KVETKOVA, L., SHEN, Z.J., Transformation of austenite to duplex austenite-ferrite assembly in annealed stainless steel 316l consolidated by laser melting, Journal of Alloys and Compounds, **633**, pp. 463–469, 2015.
19. LIU, L., DING, Q., ZHONG, Y., ZOU, J., WU, J., CHIU, Y.-L., LI, J., ZHANG, Ze, YU, Q., SHEN, Z., Dislocation network in additive manufactured steel breaks strength–ductility trade-off, Materials Today, **21**, 4, pp. 354–361, 2018.
20. ZILETALA, M., DUREJKO, T., POLANSKI, M., KUNCE, I., PLOCINSKI T., ZIELINSKI, W., LAZINSKA, M., STLEPNIOWSKI, W., CZUJKO, T., KURZYDLOWSKI, K.J., BOJAR Z., The microstructure, mechanical properties and corrosion resistance of 316l stainless steel fabricated using laser engineered net shaping, Materials Science and Engineering: A, **677**, pp. 1–10, 2016.
21. ZHANG, K., WANG, S., LIU, W., SHANG, X., Characterization of stainless steel parts by laser metal deposition shaping, Materials and Design, **55**, pp. 104–119, 2014.
22. GHOSH, A., GURAO, N.P., Effect of crystallographic texture on the planar anisotropy of ratcheting response in 316 stainless steel sheet, Materials and Design, **109**, pp. 186–196, 2016.